Soft robotic patient-specific hydrodynamic model of aortic stenosis and ventricular remodeling

Luca Rosalia[1,2,3,4], **Caglar Ozturk**[2], **Debkalpa Goswami**[2,5,6], **Jean Bonnemain**[2,7], **Sophie X. Wang**[2,8], **Benjamin Bonner**[3,4], **James C. Weaver**[9], **Rishi Puri**[10], **Samir Kapadia**[10], **Christopher T. Nguyen**[3,4,10,11,*], **Ellen T. Roche**[2,12,*]

[1]Health Sciences and Technology Program, Harvard–Massachusetts Institute of Technology, Cambridge, MA, USA.

[2]Institute for Medical Engineering and Science, Massachusetts Institute of Technology, Cambridge, MA, USA.

[3]Cardiovascular Research Center, Massachusetts General Hospital, Charlestown, MA, USA.

[4]A.A. Martinos Center for Biomedical Imaging, Massachusetts General Hospital, Charlestown, MA, USA.

[5]Department of Health Sciences and Technology, ETH-Zürich, Zürich, Switzerland.

[6]Institute of Robotics and Intelligent Systems, ETH-Zürich, Zürich, Switzerland.

[7]Department of Adult Intensive Care Medicine, Lausanne University Hospital and University of Lausanne, Lausanne, Switzerland.

[8]Department of Surgery, Beth Israel Deaconess Medical Center, Boston, MA, USA.

[9]Wyss Institute for Biologically Inspired Engineering, Harvard University, Boston, MA, USA.

[10]Department of Cardiovascular Medicine, Heart, Vascular and Thoracic Institute, Cleveland Clinic, Cleveland, OH, USA.

[11]Cardiovascular Innovation Research Center, Heart, Vascular, and Thoracic Institute, Cleveland Clinic, Cleveland, OH, USA.

[12]Department of Mechanical Engineering, Massachusetts Institute of Technology, Cambridge, MA, USA.

Abstract

Aortic stenosis (AS) affects about 1.5 million people in the United States and is associated with a 5-year survival rate of 20% if untreated. In these patients, aortic valve replacement is performed to restore adequate hemodynamics and alleviate symptoms. The development of next-generation prosthetic aortic valves seeks to provide enhanced hemodynamic performance, durability, and long-term safety, emphasizing the need for high-fidelity testing platforms for these devices. We propose a soft robotic model that recapitulates patient-specific hemodynamics of AS and secondary ventricular remodeling which we validated against clinical data. The model leverages 3D-printed replicas of each patient's cardiac anatomy and patient-specific soft robotic sleeves to recreate the patients' hemodynamics. An aortic sleeve allows mimicry of AS lesions due to degenerative or congenital disease, whereas a left ventricular sleeve recapitulates loss of ventricular compliance and diastolic dysfunction (DD) associated with AS. Through a combination of echocardiographic and catheterization techniques, this system is shown to recreate clinical metrics of AS with greater controllability compared with methods based on image-guided aortic root reconstruction and parameters of cardiac function that rigid systems fail to mimic physiologically. Last, we leverage this model to evaluate the hemodynamic benefit of transcatheter aortic valves in a subset of patients with diverse anatomies, etiologies, and disease states. Through the development of a high-fidelity model of AS and DD, this work demonstrates the use of soft robotics to recreate cardiovascular disease, with potential applications in device development, procedural planning, and outcome prediction in industrial and clinical settings.

INTRODUCTION

Aortic stenosis (AS) is the narrowing of the aortic valve orifice due to reduced mobility of the valve leaflets. It arises as a result of inflammatory processes akin to those driving atherosclerosis, whereby endothelial damage due to mechanical stress and other biological processes induces fibrosis, thickening, and calcification of the valve leaflets (1, 2). Although AS affects the elderly population disproportionately, its onset and progression can be markedly accelerated by existing underlying congenital defects, such as bicuspid aortic valve (BAV) disease, which occurs when two aortic valve leaflets are fused together (3). Hemodynamically, the narrowing of the aortic valve orifice gradually leads to elevated transaortic pressure gradients (4, 5). The increased afterload (or pressure overload) results in higher left ventricular (LV) systolic pressures and a reduction in the volume ejected at each heartbeat [stroke volume (SV)], leading to drops in cardiac output and the onset of symptoms such as angina and exertional syncope (6, 7). In two-thirds of patients with AS, pressure overload drives LV remodeling, resulting in loss of LV compliance and eventually in diastolic and/or systolic dysfunction (8-10). This complication of AS causes higher mortality and rehospitalization rates after aortic valve replacement and may eventually lead to heart failure (11-13).

AS currently affects about 1.5 million people in the United States and is associated with a 5-year survival rate of 20% from the onset of symptoms if untreated (14, 15). To date, there are no effective pharmacological treatments for AS, and it is estimated that 80,000 to 85,000 aortic valve replacement procedures are performed every year in the United States (16, 17). The prosthetic aortic valve market (valued at $6.9 billion in 2021) is rapidly expanding and is projected to reach $19.7 billion by 2031 (18). Next-generation prosthetic aortic valves

are currently under development, aiming to enhance hemodynamic performance, durability, and long-term safety (19). Unfortunately, the majority of hydrodynamic models currently used for functional evaluation of prosthetic valves rely on rigid, idealized components and fail to recreate patient-specific anatomies and hemodynamics (20). The limitations of current models emphasize the need for high-fidelity patient-specific platforms that meet the increasingly rigorous International Standard guidelines for the evaluation of cardiovascular implants (21, 22).

Recently, hydrodynamic platforms that integrate patient-specific aortic replicas have been developed for studies of congenital heart disease (23), aortic dissection (24, 25), and AS (26, 27). Kovarovic *et al.* (27) proposed a patient-specific model that integrates molded replicas of patient-specific aortic root and calcific valve geometries obtained from computed tomography (CT) data with a rigid pulse duplicator system. Similarly, Haghiashtiani *et al.* (28) combined image-guided aortic root models with a rigid pulsatile pumping system. In their work, they leveraged the multimaterial three-dimensional printing (MM3DP) approach first demonstrated by Hosny *et al.* (29) to manufacture anatomical models of calcified valves, with the advantage of enhanced prototype versatility compared with molding techniques. Nevertheless, the performance of these hydrodynamic models is largely dependent on the availability of biomechanically relevant 3D-printable polymers and the fidelity of the leaflet reconstructions. Hence, although these multimaterial 3D-printed heart valve models can be valuable in understanding the effects of calcifications on leaflet flexibility for transcatheter aortic valve replacement (TAVR) valve sizing applications (29), the differences between the intrinsic mechanical properties of the flexible materials that are used in commercial multimaterial 3D printers and those of the native heart valves can greatly compromise their ability to reliably recapitulate patient-specific hemodynamics.

Because of these potentially compounding errors and the inherent lack of real-time tunability of the as-fabricated 3D-printed valve geometries to compensate for these differences, several design-manufacturing-testing iterations would be required to obtain a high-fidelity hydrodynamic system, hindering the translatability of these models to clinical or industrial settings, which can critically rely on rapid turnaround times. Furthermore, by relying on traditional pumps or pulse duplicators, these systems are unable to model diastolic dysfunction (DD) caused by LV remodeling processes secondary to AS, which is observed in most of these patients, severely limiting the clinical relevance of these models.

Leveraging our previous work, in which we demonstrated the ability of a non–patient-specific aortic sleeve to recreate the hemodynamics of AS in a porcine model (30), we propose a soft robotics–enabled 3D-printed anatomical hydrodynamic system that is capable of recreating the hemodynamics of AS and congenital defects in a patient-specific fashion. In addition, using an analogous design workflow, we developed a patient-specific soft robotic LV sleeve that allows us to mimic changes in cardiac function observed in these patients, simulating longitudinal disease progression. We demonstrate that our soft robotic aortic sleeve can be controlled to recreate patient-specific hemodynamics of AS more accurately than current methods. Moreover, we showcase the ability of our model to mimic DD resulting from loss of LV compliance and to predict hemodynamic changes associated with treatment. This soft robotics–enabled model of both aortic and LV hemodynamics of

relevance in AS demonstrates the advantage of increased tunability over more traditional approaches, paving the way toward high-fidelity testing platforms for the evaluation of cardiac devices, personalized device selection, and outcome prediction.

RESULTS

Study workflow and architecture of the soft robotic model of AS and DD

We retrospectively selected 15 patients with a diagnosis of AS who had undergone transthoracic or transesophageal echocardiography or a combination thereof, as well as CT imaging for hemodynamic and anatomic evaluation. Our patient cohort had a broad spectrum of functional and structural characteristics relevant to AS, as summarized in Table 1. In this study population of 15 patients (six females; age, 78 ± 13 years; body surface area range, 1.67 to 2.23 m^2), the aortic annular diameter ranged from 22 to 32 mm. Four of the selected patients had a BAV anatomy, 6 were diagnosed with severe AS, 14 showed some evidence of aortic regurgitation, 8 displayed thickening of the LV wall, and 4 had an LV ejection fraction (LVEF) lower than 40% (31). Further details can be found in table S1.

Figure 1 summarizes the workflow and overall architecture of our model developed on the basis of patient hemodynamics and imaging. Clinical data, including CT, echography, and catheterization data, were obtained from patients with AS (Fig. 1A). We first segmented the CT images to create 3D anatomic models of patients' LVs and aortas (Figs. 1B and 2A), which we 3D-printed with a soft elastomeric photopolymer resin (Fig. 1C and fig. S1). We then used CT images to design patient-specific soft robotic LV and aortic sleeves (Fig. 1C). When combined with the patient-specific 3D models and our in vitro hydrodynamic model (Fig. 1D and fig. S2), the soft robotic LV sleeve provided the contractile force necessary to generate patient-specific systolic pressure and flows, as well as modulation of LV compliance seen in the spectrum of pressure overload, whereas the soft robotic aortic sleeve provided morphologic mimicry and recapitulation of patient-specific hemodynamics (movie S1). Ultimately, this personalized model allowed for testing of hemodynamic changes induced by TAVR under different conditions (Fig. 1D). An overview of the workflow, main findings, and applications of our model is described in Movie 1.

The platform designed and developed in this work is ultimately intended for high-fidelity testing and evaluation of medical devices for AS, procedural planning, and outcome prediction, as well as product selection personalized to each patient's anatomy, hemodynamics, and disease state. Hence, we demonstrated its potential utility by implanting a TAVR and conducted retrospective clinical validation in a subset of our study cohort.

Soft robotic aortic sleeve recapitulates patient-specific morphology of AS and congenital valvular defects

The soft robotic aortic sleeve enabled us to recreate the valve lesion morphology of each individual patient with high fidelity. Figure 2A shows a comparison, for each patient, of the aortic valve cine CT images and of the aortic cross sections of our model under actuation of the aortic sleeve, captured using an endoscopic camera in the system. These images demonstrate that our sleeve can qualitatively recreate a range of patient-specific anatomies,

including those of degenerative AS and BAV, with high accuracy. We then superimposed the CT and aortic sleeve images of the orifice area for each patient and calculated the Sørensen-Dice similarity coefficient (DSC) for a quantitative comparison (32). An example of superimposed CT and aortic sleeve images is illustrated in Fig. 2B, where the white area denotes the region of perfect overlap between the two images, whereas the cyan or red areas denote regions of image mismatch. All images used for calculation of DSC score can be found in fig. S3. The average DSC across the 15 patients modeled was 0.88 ± 0.05 (Fig. 2C), demonstrating the overlap between native valve morphology seen on CT and our personalized aortic sleeve.

Patient-specific aortic sleeves are tuned to recreate AS hemodynamics

By recreating patient-specific aortic valve anatomies, our soft robotic aortic sleeve was able to induce aortic valve hemodynamics as measured via echography. We validated our model by comparing the clinical parameters measured in these patients for AS evaluation with those obtained by our system. We also compared the performance of our model with one containing valves fabricated using the MM3DP approach by Hosny *et al.* (29), whereby CT images were used to generate 3D-printed patient-specific aortic sinus and leaflet anatomies in tandem with rigid calcium-like patterns corresponding to the patients' mineralized nodules. To document the performance of the multimaterial 3D-printed valves in a similar context, we merged them with the patient-specific model of the LV and ascending aorta to perform functional hydrodynamic studies (fig. S4). Figure 3A shows images of the LV and aortic sleeves of the soft robotic model, highlighting their main components, including the inflatable pockets and inelastic fabric. It also shows the multimaterial 3D-printed valves with calcium-like nodules and their corresponding CT data for the subset of patients used for hydrodynamic validation (patients 7 to 11).

Our model accurately recapitulated the critical hemodynamic parameters of AS with high accuracy for each patient. For our analysis, we considered the mean (P_{mean}; Fig. 3B) and maximum transaortic pressure gradients (P_{max}; Fig. 3C), the peak aortic flow velocity (v_{max}; Fig. 3D), and the SV (Fig. 3E). The soft robotic model more closely matched the clinical targets, with a compounded average absolute deviation of $7.7 \pm 1.5\%$ for all metrics compared with the MM3DP approach ($13.9 \pm 6.2\%$). Specifically, we found variations of $P_{\text{mean}} = 6.3 \pm 5.6\%$ versus $10.5 \pm 11.3\%$, $P_{\text{max}} = 9.8 \pm 3.6\%$ versus $11.3 \pm 3.5\%$, $v_{\text{max}} = 7.5 \pm 1.9\%$ versus $10.6 \pm 4.2\%$, and SV $= 7.5 \pm 1.9\%$ versus $23.3 \pm 8.3\%$, for the soft robotic ($n = 15$) and multimaterial 3D-printed ($n = 5$) models. Representative color flow mapping and continuous wave Doppler images illustrating the corresponding aortic velocity profiles obtained for the soft robotic model and its MM3DP analog are depicted in Fig. 3 (F and G). Movie S2 shows B-mode videos of the two techniques. Overlaid LV pressure (LVP) and aortic pressure (AoP) waveforms for representative cases of healthy physiology and of mild (patient 15; $P_{\text{max}} = 32.0 \pm 1.6$ mmHg), moderate (patient 8; $P_{\text{max}} = 58.0 \pm 3.2$ mmHg), and severe (patient 2; $P_{\text{max}} = 89.2 \pm 1.6$ mmHg) AS are illustrated in Fig. 3H. The graph highlights changes in P_{max} associated with various disease severities. LVP and AoP tracings and continuous wave Doppler images for all patients (patients 1 to 15) are displayed in figs. S5 and S6.

Dynamic tuning of soft robotic LV sleeve mimics loss of ventricular compliance and DD secondary to AS

We customized the LV sleeve to the patient's anatomy and actuated it to recreate anatomical filling, emptying, and wall motion during diastole (Fig. 4A) and systole (Fig. 4B and movie S3). By tuning the actuation pressures of the LV sleeve during diastole, LV compliance and diastolic function can be modulated (Fig. 4C). This approach allows us to recreate elevations in the LV end-diastolic pressure (LVEDP; Fig. 4D) associated with concentric remodeling secondary to AS.

We simulated the hemodynamics of four patients with reported LV catheterization data (patients 10 to 13; see table S1) to demonstrate the ability of the soft robotic system to recreate cardiac hemodynamics of patients with different degrees of LV remodeling. Figure 4E illustrates LV pressure-volume (PV) loops of the healthy physiology and of two representative patients with DD (patients 10 and 12), highlighting changes in the end-diastolic PV relationship (EDPVR) due to remodeling. Analogously, Fig. 4F shows overlaid LVP and AoP waveforms for the healthy physiology and representative cases of mild (patient 10; LVEDP = 18.0 ± 1.0 mmHg), moderate (patient 13; LVEDP = 27.6 ± 1.4 mmHg), and severe (patient 12; LVEDP = 35.4 ± 1.9 mmHg) DD.

Measurements of the LV and aortic hemodynamics—including LVEDP (Fig. 4G), systolic LVP (LVP$_S$; Fig. 4H), LVEF (Fig. 4I), systolic AoP (AoP$_S$; Fig. 4J), diastolic AoP (AoP$_D$; Fig. 4K), and mean AoP (AoP$_m$; Fig. 4L)—and comparison with clinical data further corroborate the ability of our soft robotic system to create a high-fidelity model of each patient's LV and aortic hemodynamics. For each of these metrics, we computed the absolute deviation from the corresponding clinical values, obtaining $1.2 \pm 0.9\%$ (LVEDP), $0.6 \pm 0.5\%$ (LVP$_S$), $3.8 \pm 2.2\%$ (LVEF), $4.6 \pm 4.3\%$ (AoP$_S$), $2.1 \pm 2.0\%$ (AoP$_D$), and $2.8 \pm 2.6\%$ (AoP$_m$) ($n = 4$ patients). Overall, this approach showcases the ability of our platform to recreate LV hemodynamics and changes in LV compliance associated with remodeling processes and DD secondary to AS with high fidelity.

Soft robotic platform predicts the hemodynamic outcome of TAVR implantation in patients with AS

We demonstrated use of our model for the evaluation of post-TAVR hemodynamics in a subset of patients via implantation of the self-expanding Evolut R (Medtronic, Minneapolis, MN) and the balloon-expandable SAPIEN 3 (Edwards Lifesciences, Irvine, CA) prostheses. Figure 5A shows a schematic of the Evolut R valve deployed through the distal end of the 3D-printed anatomy and a detail of the valve outflow. A B-mode video of an Evolut R valve implanted in the model is shown in movie S2. Changes in LVP and AoP waveforms and in the LV PV loop for a representative case (patient 6) of pre- and post-TAVR implantation are illustrated in Fig. 5 (B and C). These graphs highlight unloading of the LV, with a drop in peak LVP and a raise in SV and in the aortic pulse pressure. Pre- and post-TAVR LVP and AoP waveforms for all patients in this study are shown in fig. S7.

Using our clinical database, we validated post-TAVR hemodynamic data for patients with an appropriately sized valve (patients 3, 4, 6, 7, 11, and 14). Figure 5 (D and E) shows

a comparison between the clinical data and the model for both pre- and post-TAVR implantation for P_{mean} and P_{max}. We found absolute deviations of $P_{mean} = 4.3 \pm 3.7\%$ and $P_{max} = 15.7 \pm 13.9\%$ from postimplantation clinical data, suggesting that our model can accurately predict hemodynamic changes due to treatment. Further, we computed changes in effective orifice area (EOA; Fig. 5F; 0.9 ± 0.2 cm^2 versus 1.8 ± 0.4 cm^2), v_{max} (Fig. 5G; 3.9 ± 0.7 m/s versus 0.7 ± 1.4 m/s), and SV (Fig. 5H; 53.2 ± 12.0 ml versus 76.4 ± 7.2 ml) pre-versus postimplantation. All pre- and post-TAVR implantation data are summarized in table S2.

Last, we investigated the degree of paravalvular leak and regurgitation in a group of patients receiving an undersized valve versus recipients of an appropriately sized prosthesis. Figure 5I illustrates representative color flow mapping Doppler images for the two groups, highlighting more substantial paravalvular leak associated with undersized implants. Analogously, calculation of the aortic regurgitation index (ARI) through catheterization shows less optimal TAVR performance for the undersized group than for the group given appropriately sized valves (Fig. 5J; ARI = 22.0 ± 4.7 versus 45.4 ± 7.8; $P = 9.8 \times 10^{-5}$). These findings are consistent with the literature associating lower values of ARI with higher mortality in patients with aortic valve disease (33, 34).

DISCUSSION

In this work, we present the development of a patient-specific hydrodynamic model driven by tunable soft robotic tools, of relevance in AS and LV remodeling. We demonstrated the ability of this model to recreate patient-specific anatomies of degenerative stenotic aortic valves and of congenital BAV disease (Fig. 2A). Biomechanical mimicry of the AS lesion is paramount to accurately recreate local flow hemodynamics in a high-fidelity platform. In this work, calculation of the DSC between the model and CT images demonstrated that the patient-specific aortic sleeve can achieve enhanced mimicry (DSC = 0.88 ± 0.05) compared with commercial aortic banding techniques (DSC = 0.47) and nonspecific aortic sleeves (DSC = 0.72) (30). Furthermore, our platform recapitulates the hemodynamics of AS (Fig. 3, B to E) with greater accuracy compared with other systems, with a mean absolute deviation equal to $7.7 \pm 1.5\%$ ($n = 15$), which is lower than that achieved via the use of multimaterial 3D-printed valves produced on commercial multimaterial 3D printers ($13.9 \pm 6.2\%$, $n = 5$; Fig. 3, B to E).

In the context of developing a clinically relevant hydrodynamic testing platform, the incorporation of molded or multimaterial 3D-printed valves depends more heavily on the resolution of the patients' CT images and on the quality of image segmentation when compared with our more adaptable soft robotic platform. In these systems (molded and MM3DP), any mismatch between the patients' anatomies and the aortic root replicas can only be improved by manual editing of the digital valvular geometries. This time-consuming iterative process compromises the utility of these hydrodynamic models in a clinical setting, where TAVR procedures are often performed within a day from initial CT imaging. Conversely, in our soft robotic model, actuation can be tuned in real time to obtain high-fidelity mimicry of the patients' hemodynamics by modulating the aortic root diameter (Fig. 3F). The controllability of molding or MM3DP-based hydrodynamic models is further

limited by differences between the mechanical properties of the manufactured valve material and those of the native leaflet tissue. Although the investigation of valve kinetics was beyond the scope of this work, the dynamics of the aortic sleeve in this model could be controlled to mimic the motion of stenotic valve leaflets, as previously demonstrated (30). Unlike other models, our platform was also able to recreate the anatomies of congenital valvular defects, such as BAV (patients 12 to 15 in Figs. 2A and 3, B to E), which are a primary driver of AS in the younger population (3). The MM3DP approach developed by Hosny *et al.* (29) relies on an algorithm that computes an idealized geometry of a tricuspid aortic valve from CT image landmarks and is yet to be broadened to recreate BAV anatomies or other congenital aortic valve defects.

Integration of a controllable soft robotic LV sleeve (Figs. 3A and 4, A and B) is a critical step toward the development of clinically relevant hydrodynamic models of AS and other cardiovascular conditions. Traditional hydrodynamic models leverage displacement-control pumps, which eject a prescribed amount of volume into the circulation. First, this is not representative of cardiac physiology. Second, it makes recreating the hemodynamics of conditions where the afterload is altered challenging. In the context of AS, these systems would not be able to capture drops in SV associated with a higher afterload (Fig. 3E), leading to overestimated values of flow velocities predicted by the continuity equation (Fig. 3, D and G) (35, 36). Conversely, by mimicking the biomechanics of the native heart in both physiology and disease, we overcame these limitations and recreated both pressure and flow in a more clinically relevant manner (Fig. 4) (37-40).

The personalized LV sleeve design enabled us to modulate LV compliance to simulate the hemodynamic effects of cardiac remodeling secondary to AS in a patient-specific manner (Fig. 4C). In particular, we were able to simulate alterations in LV filling pressures and DD in patients with various degrees of remodeling due to pressure overload (Fig. 4, D to M). This model of modulation of ventricular compliance can be used to represent different states of disease progression, which has not been shown previously. Because thickening and subsequent decrease of LV compliance are estimated to occur in more than two-thirds of patients with AS (8), it is paramount that preclinical models of AS can correctly recapitulate changes in LV diastolic biomechanics and hemodynamics associated with pressure overload.

Our model was shown to predict hemodynamic changes associated with treatment with established TAVR prostheses. We used clinical transaortic pressure gradient data in a subset of patients to retrospectively validate our system as a platform for hemodynamic outcome prediction (Fig. 5, D and E). Further, we measured changes in LVP and AoP (Fig. 5B), LV PV loops (Fig. 5C), EOA (Fig. 5F), v_{max} (Fig. 5G), and SV (Fig. 5H) resulting from simulating intervention in our model. We found that changes measured in this study are consistent with the literature of large-population studies of TAVR outcome (41-43).

This research thus has the potential to enable medical device companies to test and optimize their devices reliably across a spectrum of clinical cases, broadening the usability of devices to those patients for whom current TAVR designs are not suitable, beneficial, or safe to use. In the clinic, it would provide physicians with a platform for device selection, procedural planning, and outcome prediction. Furthermore, it may provide clinicians with

a tool to improve techniques for TAVR delivery to minimize risk of coronary obstruction or valve migration and to optimize device selection for patients with complex anatomies or sizes that fall between recommended use ranges for a given device. Last, it may help identify subgroups for which TAVR could be beneficial and performed safely within patient populations, such as patients with BAV disease, who are currently ineligible for TAVR and have been traditionally excluded from major trials comparing surgical versus transcatheter interventions (44, 45).

The continuous development of new techniques for the treatment of AS accentuates the need for high-fidelity systems that can be used as training platforms (46, 47). In vitro models developed to date lack the anatomical and functional accuracy required to make them a suitable alternative to in vivo models, which remain difficult to realize in large numbers due to ethical concerns and elevated costs (48, 49). The model proposed in this work has the potential to contribute to advances in TAVR interventional training. First, our patient-specific approach allows for enhanced anatomical accuracy and enables the recapitulation of morphologies of a variety of AS lesions and congenital defects of the aortic valve that other systems are unable to mimic. Furthermore, our model provides the advantage of recreating aortic hemodynamics and secondary LV dysfunction with elevated controllability, potentially allowing simulation of changes in cardiac function, because they may occur during intervention (50). The usability of this model as a training platform can be enhanced further by augmenting anatomical fidelity through integration of 3D-printed elements modeling vascular access points for TAVR procedures.

Despite the many advantages offered by our hydrodynamic platform, there are three main limitations that should be considered. First, the position of the aortic sleeve on the ascending aorta may affect the compliance of the 3D-printed model. In particular, the aortic sleeve causes a drop in distension of the aortic segment corresponding to the position of the sleeve. In addition, any aortic segments that are proximal to the aortic sleeve will experience LV (rather than aortic) pressures, which are elevated in AS. Together, these factors may lead to local differences in aortic distension compared with those measured physiologically. Second, although our model was shown to capture LVPs and flows (Fig. 4C) with high accuracy compared with other hydrodynamic models (51-53), the isovolumic regions of LV PV loops display a nonzero net flow toward or outside of the LV. This observation is a result of the position of the aortic flow probe, which could only be placed distal to the aortic valve plane because of the irregular geometry of the 3D-printed aortic anatomies. Last, the dataset used in this study did not provide indications of the patients' systolic-diastolic ratio, which limited our ability to modulate the exact dynamics of ventricular contraction and may have influenced hemodynamic measurements.

Improvements to this study would involve automation of the sleeve design process and 3D-printing techniques to further reduce the manufacturing time of the patients' replicas and to maximize clinical utility. Furthermore, obtaining access to a broader spectrum of transcatheter valve prostheses and a larger clinical database would permit a prospective validation of our TAVR prediction study. Last, the utilization of alternative 3D-printing materials with enhanced optical properties would enable patient-specific 4D flow visualization and turbulence formation through particle image velocimetry studies.

Eventually, use of this soft robotics–driven model may be broadened to simulate the hemodynamics of other valvular heart diseases and conditions that affect LV function, including restrictive cardio-myopathies and heart failure—both with reduced and preserved ejection fraction. We are hopeful that this model can pave the way toward high-fidelity patient-specific tunable models with a translational potential poised to improve clinical care of the millions of people worldwide affected by AS and other cardiovascular conditions.

MATERIALS AND METHODS

Study design

Anonymized CT and echocardiographic clinical data from 15 patients with AS were obtained retrospectively via Institutional Review Board approval at the Massachusetts General Hospital. Using echocardiographic measurements of the LV diameter during systole and diastole, we screened for chest CT images acquired during diastole. This approach allowed us to design the geometry of our patient-specific soft robotic LV sleeve in its preactuation state. Conversely, images of the aortic valve were taken during peak systole from the patients' aortic valve cine images, thus enabling the development of patient-specific soft robotic aortic sleeves that could recreate the morphology of the stenotic leaflets during systole. Each patient's 3D-printed anatomical model was integrated with the LV and aortic sleeves into a hydrodynamic flow loop, with added pressure and flow sensors and an endoscopic camera for hemodynamic evaluation. Hemodynamic parameters relevant in AS were measured using PV catheters, flow probes, an endoscopic camera, and continuous wave and color flow mapping Doppler, as described below. Results were compared with the patients' clinical data and established methods based on MM3DP. Last, hemodynamic changes due to implantation of Evolut R (Medtronic, Minneapolis, MN) and SAPIEN 3 (Edwards Lifesciences, Irvine, CA) valves were evaluated.

Patient CT data segmentation and 3D printing of cardiac and aortic vascular anatomies

CT and aortic valve cine images (slice thickness $t = 1.0$ to 1.5 mm, x-ray depth $D = 10$ mm) were segmented on Mimics Research software (v.21.0.0.406, Materialise, NV) by thresholding, multiple slice editing, and autointerpolation. The geometrical axes of the cine images were reoriented to ensure visualization of the valve leaflets orthogonal to the direction of flow.

For each patient, the 3D anatomy of the LV and aorta (ascending through descending segment) was exported from the CT images as a shell stereolithography (STL) file with wall thickness equal to 1.3 mm. A thickness value lower than that of the human aorta was chosen to compensate for any mismatch in mechanical properties between the 3D-printing photopolymer resin (Elastic 50A, Formlabs, Somerville, MA) and those of the native aorta (fig. S1). Because the mechanics of the LV are defined by actuation pressures of the LV sleeve, a thickness value of 1.3 mm for the 3D-printed LV wall was chosen for ease of manufacturing. Each STL file was then imported to Preform software (v3.21, Formlabs), and the architecture of the support material was manually adjusted to avoid any overhang and to minimize the presence of internal support material. Each anatomy was then printed on a Form 3B STL 3D printer (Formlabs) with a layer thickness of 0.1 mm.

LV and aortic sleeve design and manufacturing

Each anatomical (STL) LV model was used for the design of a patient-specific soft robotic LV sleeve in SolidWorks (2019, Dassault Systèmes, Vélizy-Villacoublay, France). The outer surface of the LV was offset by 10 mm to generate guide tracings for the sleeve geometry, and the tracings were divided into four circumferential quadrants (each about 90° apart). These quadrants were flattened to a plane to create the contours of the molds for manufacturing. The flat tracings were then extruded by the same offset (10 mm), and each mold was 3D printed from a rigid photopolymer (Veroblue, Stratasys, Eden Prairie, MN) with an inkjet-based Objet30 3D printer (Stratasys, Eden Prairie, MN). Similarly, the contours of the aortic valve leaflets were exported from CT images and converted into flat geometries, which were then extruded and 3D-printed for manufacturing of the aortic sleeve.

Analogously to the manufacturing technique previously described by our group (30, 54), for each of the four LV molds and three aortic molds (or two for bicuspid valve anatomies) per patient, two sheets of thermoplastic polyurethane (TPU; HTM 8001-M 80A shore polyether film, 0.012 inches in thickness; American Polyfilm Inc., Branford, CT) were vacuum-formed (Dental Vacuum Former, Yescom, City of Industry, CA) into the shape of the molds. Each pair of TPU sheets was then heat-sealed at 320°F for 8 s on a heat press transfer machine using negative acrylic molds to create enclosed and inflatable geometries. For each sleeve, these inflatable pockets were then heat-sealed using a similar process as that described above to a 200-Denier TPU-coated fabric (Oxford fabric, Seattle fabrics Inc., Seattle, WA), which was designed to fit around their respective LV or aortic anatomy. Further, holes were opened through the fabric on one side of each of the pockets to connect soft tubes [latex rubber $^1/_{16}$-inch inner diameter (ID) and $\frac{1}{8}$-inch outer diameter (OD) tubing; McMaster-Carr, Elmhurst, IL] as actuation lines through PVC (polyvinyl chloride) connectors (polycarbonate plastic double-barbed tube fitting for $^1/_8$-inch tube ID; McMaster-Carr, Elmhurst, IL).

A 3D-printed (Objet30, Stratasys) rigid skeleton with four arms (one for each pair of adjacent pockets of the LV sleeve) was designed to secure each LV sleeve to the corresponding 3D-printed geometry. A belt-like securing mechanism with Velcro adhesive was integrated in the design of the fabric of each aortic sleeve to guarantee secure attachment around the 3D-printed aorta (Fig. 3A).

3D printing of calcified valves

In this work, the MM3DP approach developed by Hosny *et al.* (29) was optimized for hydrodynamic testing and used for comparison with our model. We used the algorithm developed in their work to generate the aortic valve leaflet geometries from landmarks of abdominal CT images with superimposed calcium-like nodules. However, instead of limiting the vascular anatomy to the aortic sinus, we integrated the valve leaflets and nodules into the entire LV and aortic (through the aortic arch segment) anatomies. First, this approach allowed us to conduct functional tests of their model of AS. Second, it enabled us to integrate their approach with our strategy of LV actuation, allowing for a fairer comparison between the two models of AS. The LV, aorta, aortic valve leaflets, and calcium nodules

were printed simultaneously using an Objet 500-Connex3 3D printer (Stratasys) using the same printing techniques as described in the original publication (29). To do this, we created a small (2 to 5 mm in diameter) hole in proximity to the LV apex to remove any support material laid down during the manufacturing process. The hole was then sealed using the same resin material, and ultraviolet light was applied manually.

Patient-specific hydrodynamic studies

For each patient, a closed loop was set up for hydrodynamic studies (viscosity of medium, $\mu = 1.0$ cP) (22). The loop was assembled by connecting the 3D-printed anatomy to a series of soft PVC plastic tubing ($\frac{3}{8}$- to $\frac{5}{8}$-inch ID, $\frac{5}{8}$- to 1-inch OD; McMasterr-Carr), two variable-resistance ball valves to mimic arterial and venous resistance, and two custom-made acrylic compliance chambers to recreate peripheral compliance. A unidirectional mechanical valve (Regent bileaflet mechanical prosthesis, 19AGN-751 standard cuff; Abbott Laboratories, Chicago, IL) was connected in proximity to the venous system. Two clamp-on perivascular flow probes (PS series, Transonic, Ithaca, NY) were used to measure flow immediately distal to the descending aorta (LV outflow) and distal to the surgical valve in the LV (LV inflow). The flow probes were connected to a two-channel flowmeter console (400 series, Transonic), which was, in turn, connected to an eight-channel Powerlab system (ADInstruments, Sydney, Australia) for data acquisition and recording. Two straight-tip 5F PV catheters were inserted through two adjustable catheter connectors to measure pressures at the LV and at the ascending aorta, distal to the aortic sleeve. The catheters were connected to a Transonic ADV500 PV System and to the Powerlab (ADInstruments). Given the mismatch in electrical impedance between the 3D-printed material and that of the native cardiac tissue, the PV catheters could not be used to reliably measure volumes inside the LV. An endoscopic camera was inserted in the system to visualize the cross-sectional profiles of the aorta during actuation for subsequent calculations of the valve EOA.

The system was actuated pneumatically through the soft robotic LV sleeve, which was connected to a control box and associated graphical user interface (GUI), where input pressure tracings could be defined (Fig. 4C). The aortic sleeve was actuated hydraulically using a syringe pump (70-3007 PHD ULTRA Syringe Pump Infuse/Withdraw, Harvard Apparatus, Cambridge, MA). The actuation pressures and volumes of the soft robotic sleeves were modulated to achieve the values of SV and $P_{\max}$ for each individual patient, as well as LV and AoP values when known. Systolic and diastolic actuation pressures of the LV sleeves ranged between 8 to 13 psi and 0 to 6psi for systole and diastole, respectively, whereas actuation volumes equal to 20 to 40 ml were used for actuation of the aortic sleeves.

Echocardiographic evaluation

The Epiq CVx cardiovascular ultrasound system (Philips, Amsterdam, Netherlands) was used in tandem with the X5-1 transducer (Philips) for echocardiographic evaluation of each patient-specific model to assess the degree of AS and, in some instances, LV function and paravalvular leak. Because the transaortic pressure gradients and the EOA could be more accurately measured using the PV catheters and the endoluminal camera, respectively, echocardiography was primarily used to compute the peak flow velocity ($v_{\max}$) through the aortic valve (Figs. 3D and 5G and fig. S6). The probe was positioned directly on the

3D-printed geometry, leveraging the anatomical curvature between the ascending aorta and proximal arch to align the ultrasonic beam with the direction of flow for continuous wave Doppler imaging. Tracings of the aortic flow velocity were obtained, and the peak value of each tracing (v_{max}) was calculated. In a subset of patient models, color flow mapping Doppler images were obtained for visualization of the flow through the soft robotic aortic sleeve and stenotic multimaterial 3D-printed valves for comparison. In addition, 2D movies of the LV in long-axis view, of the multimaterial 3D-printed valve, and of the SE valve prosthesis (Evolut R, Medtronic) were recorded to visualize actuation of the soft robotic LV sleeve (Fig. 4, A and B) and mobility of the multimaterial 3D-printed and TAVR leaflets. Last, color flow mapping Doppler images were taken to provide a qualitative comparison of the degree of paravalvular leak between the patient models with an appropriately sized and an undersized valve (Fig. 5I).

Evaluation of post-TAVR hemodynamics

A study of the differences in paravalvular leak and ARI between the undersized TAVR and appropriately sized TAVR groups was conducted by simulating implantation of valves of various sizes in patients with a spectrum of annular dimensions. We used undersized valves in patients 2, 3, 6, 7, 10, and 14 and appropriately sized valves in patients 3, 4, 6, 7, 11, and 14. The Evolut R valve (Medtronic) was delivered manually from a distal opening in the anatomy to the point of constriction or slightly supra-annularly, whereas the SAPIEN 3 valve (Edwards Lifesciences) was delivered using the Edwards transfemoral balloon catheter (Edwards Lifesciences).

In this study, we computed the ARI as per Eq. 1

$$ARI = \frac{A_oP_D - LVEDP^*}{AoP_s} 100 \qquad (1)$$

All parameters in this equation were measured from PV catheters. Other metrics, including P_{mean}, P_{max}, EOA, v_{max}, SV, LVP, LV volume (LVV), and AoP, were calculated.

Data analysis

Data were primarily visualized and acquired by LabChart (Pro v8.1.16, ADInstruments). All the input signals were filtered using the default 50-Hz band-stop filter. Signals include the LV and AoPs for calculation of the transaortic pressure gradient and the flow rates out of and into the LV for calculation of the SV and LVEF. From these data, the LVEDP, LVPs, AoP, and LVV could be extracted. Analogously, the actuation pressure of the LV sleeve was displayed and recorded on LabChart. Data analysis and visualization were performed through an automated algorithm developed on MATLAB R2020a (MathWorks, Natick, MA). Values for peak flow velocity measured using continuous wave Doppler were included in the analysis. For catheterization data, average values and SDs were calculated for $n = 10$ consecutive heart cycles after the soft robotic sleeve actuation degrees were successfully tuned to recreate the patients' cardiac and aortic hemodynamics. Echocardiography data were averaged across three heart cycles. A two-tailed t test was performed (MATLAB R2020a) to determine significance between the undersized and the correctly sized TAVR

groups (Fig. 5J) using a 95% confidence interval ($P < 0.05$). For each patient in the analysis, we considered the average ARI value calculated across five consecutive heart cycles. A Kolmogorov-Smirnov test (MATLAB R2020a) confirmed a standard normal distribution of the ARI averages within each of the two groups (Fig. 5J).

Images of the aortic cross sections were processed using the Image Processing and Computer Vision MATLAB toolbox (MATLAB R2020a) for calculation of the EOA. These images and those obtained from the patients' CT were binarized, and each pair of images (one pair per patient) was cross-registered. The rigid distortion option, enabling only translation and rotation of the moving image, was used for image registration, and the DSC was calculated for each patient model.

Supplementary Material

Refer to Web version on PubMed Central for supplementary material.

Acknowledgments:

REFERENCES AND NOTES

1. Fishbein GA, Fishbein MC, Pathology of the aortic valve: Aortic valve stenosis/aortic regurgitation. Curr. Cardiol. Rep 21, 81 (2019). [PubMed: 31278595]

2. Ternacle J, Krapf L, Mohty D, Magne J, Nguyen A, Galat A, Gallet R, Teiger E, Côté N, Clavel M-A, Tournoux F, Pibarot P, Damy T, Aortic stenosis and cardiac amyloidosis. J. Am. Coll. Cardiol 74, 2638–2651 (2019). [PubMed: 31753206]

3. Roberts WC, Ko JM, Frequency by decades of unicuspid, bicuspid, and tricuspid aortic valves in adults having isolated aortic valve replacement for aortic stenosis, with or without associated aortic regurgitation. Circulation 111, 920–925 (2005). [PubMed: 15710758]

4. Rajani R, Hancock J, Chambers JB, The art of assessing aortic stenosis. Heart 98, iv14–iv22 (2012). [PubMed: 23143121]

5. Carabello BA, Paulus WJ, Aortic stenosis. Lancet 373, 956–966 (2009). [PubMed: 19232707]

6. Gotzmann M, Hauptmann S, Hogeweg M, Choudhury DS, Schiedat F, Dietrich JW, Westhoff TH, Bergbauer M, Mügge A, Hemodynamics of paradoxical severe aortic stenosis: Insight from a pressure–volume loop analysis. Clin. Res. Cardiol 108, 931–939 (2019). [PubMed: 30737530]

7. Rosalia L, Ozturk C, Van Story D, Horvath MA, Roche ET, Object-oriented lumped-parameter modeling of the cardiovascular system for physiological and pathophysiological conditions. Adv. Theory Simul 4, 2000216 (2021).

8. Dweck MR, Joshi S, Murigu T, Gulati A, Alpendurada F, Jabbour A, Maceira A, Roussin I, Northridge DB, Kilner PJ, Cook SA, Boon NA, Pepper J, Mohiaddin RH, Newby DE, Pennell DJ, Prasad SK, Left ventricular remodeling and hypertrophy in patients with aortic stenosis: Insights from cardiovascular magnetic resonance. J. Cardiovasc. Magn. Reson 14, 50 (2012). [PubMed: 22839417]

9. Rosalia L, Ozturk C, Shoar S, Fan Y, Malone G, Cheema FH, Conway C, Byrne RA, Duffy GP, Malone A, Roche ET, Hameed A, Device-based solutions to improve cardiac physiology and hemodynamics in heart failure with preserved ejection fraction. JACC Basic Transl. Sci 6, 772–795 (2021). [PubMed: 34754993]

10. Pfeffer MA, in Atlas of Heart Failure, Colucci WS, Ed. (Current Medicine Group, London, 2002), pp. 87–101.

11. Rader F, Sachdev E, Arsanjani R, Siegel RJ, Left ventricular hypertrophy in valvular aortic stenosis: Mechanisms and clinical implications. Am. J. Med 128, 344–352 (2015). [PubMed: 25460869]

12. Barletta G, Del Bene MR, Venditti F, Pilato G, Stefàno P, Surgical aortic valve replacement and left ventricular remodeling: Survival and sex-related differences. Echocardiography 38, 1095–1103 (2021). [PubMed: 34028878]

13. Duncan AI, Lowe BS, Garcia MJ, Xu M, Gillinov AM, Mihaljevic T, Koch CG, Influence of concentric left ventricular remodeling on early mortality after aortic valve replacement. Ann. Thorac. Surg 85, 2030–2039 (2008). [PubMed: 18498815]

14. Joseph J, Naqvi SY, Giri J, Goldberg S, Aortic stenosis: Pathophysiology, diagnosis, and therapy. Am. J. Med 130, 253–263 (2017). [PubMed: 27810479]

15. Bevan GH, Zidar DA, Josephson RA, Al-Kindi SG, Mortality due to aortic stenosis in the United States, 2008-2017. JAMA 321, 2236–2238 (2019). [PubMed: 31184728]

16. Gheorghe GS, Hodorogea AS, Gheorghe ACD, Nanea IT, Ciobanu A, Medical management of symptomatic severe aortic stenosis in patients non-eligible for transcatheter aortic valve implantation. J. Geriatr. Cardiol 17, 704–709 (2020). [PubMed: 33343649]

17. Mazine A, Ouzounian M, Aortic valve replacement in young and middle-aged adults: Looking beyond the tree that hides the forest. Ann. Transl. Med 5, 92–92 (2017). [PubMed: 28275637]

18. Research and Markets, Transcatheter Heart Valve Replacement Market, Global Forecast 2022-2027, Industry Trends, Impact of COVID-19, Opportunity Company Analysis (2022).

19. Puri R, Chamandi C, Rodriguez-Gabella T, Rodés-Cabau J, Future of transcatheter aortic valve implantation — Evolving clinical indications. Nat. Rev. Cardiol 15, 57–65 (2018). [PubMed: 28836620]

20. Haaf P, Steiner M, Attmann T, Pfister G, Cremer J, Lutter G, A novel pulse duplicator system: Evaluation of different valve prostheses. Thorac. Cardiovasc. Surg 57, 10–17 (2009). [PubMed: 19169990]

21. Rosenzweig A, The growing importance of basic models of cardiovascular disease. Circ. Res 130, 1743–1746 (2022). [PubMed: 35679368]

22. International Organization for Standardization (ISO), ISO - ISO 5840-1:2021 - Cardiovascular Implants — Cardiac Valve Prostheses — Part 1: General Requirements (2021); www.iso.org/standard/77033.html.

23. Medero R, García-Rodríguez S, François CJ, Roldán-Alzate A, Patient-specific in vitro models for hemodynamic analysis of congenital heart disease - Additive manufacturing approach. J. Biomech 54, 111–116 (2017). [PubMed: 28242061]

24. Chen D, Liang S, Li Z, Mei Y, Dong H, Ma Y, Zhao J, Xu S, Zheng J, Xiong J, A mock circulation loop for in vitro hemodynamic evaluation of aorta: Application in aortic dissection. J. Endovasc. Ther 29, 132–142 (2022). [PubMed: 34342237]

25. Bonfanti M, Franzetti G, Homer-Vanniasinkam S, Díaz-Zuccarini V, Balabani S, A. Combined, A combined in vivo, in vitro, in silico approach for patient-specific haemodynamic studies of aortic dissection. Ann. Biomed. Eng 48, 2950–2964 (2020). [PubMed: 32929558]

26. Roldán-Alzate A, García-Rodríguez S, Anagnostopoulos PV, Srinivasan S, Wieben O, François CJ, Hemodynamic study of TCPC using in vivo and in vitro 4D Flow MRI and numerical simulation. J. Biomech 48, 1325–1330 (2015). [PubMed: 25841292]

27. Kovarovic BJ, Rotman OM, Parikh P, Slepian MJ, Bluestein D, Patient-specific in vitro testing for evaluating TAVR clinical performance—A complementary approach to current ISO standard testing. Artif. Organs 45, E41–E52 (2021). [PubMed: 33031563]

28. Haghiashtiani G, Qiu K, Zhingre Sanchez JD, Fuenning ZJ, Nair P, Ahlberg SE, Iaizzo PA, McAlpine MC, 3D printed patient-specific aortic root models with internal sensors for minimally invasive applications. Sci. Adv 6, eabb4641 (2020). [PubMed: 32923641]

29. Hosny A, Dilley JD, Kelil T, Mathur M, Dean MN, Weaver JC, Ripley B, Pre-procedural fit-testing of TAVR valves using parametric modeling and 3D printing. J. Cardiovasc. Comput. Tomogr 13, 21–30 (2019).

30. Rosalia L, Ozturk C, Coll-Font J, Fan Y, Nagata Y, Singh M, Goswami D, Mauskapf A, Chen S, Eder RA, Goffer EM, Kim JH, Yurista S, Bonner BP, Foster AN, Levine RA, Edelman ER, Panagia M, Guerrero JL, Roche ET, Nguyen CT, A soft robotic sleeve mimicking the haemodynamics and biomechanics of left ventricular pressure overload and aortic stenosis. Nat. Biomed. Eng 6, 1134–1147 (2022). [PubMed: 36163494]

31. Heidenreich PA, Bozkurt B, Aguilar D, Allen LA, Byun JJ, Colvin MM, Deswal A, Drazner MH, Dunlay SM, Evers LR, Fang JC, Fedson SE, Fonarow GC, Hayek SS, Hernandez AF, Khazanie P, Kittleson MM, Lee CS, Link MS, Milano CA, Nnacheta LC, Sandhu AT, Stevenson LW, Vardeny O, Vest AR, Yancy CW, 2022 AHA/ACC/HFSA guideline for the management of heart failure: A report of the American College of Cardiology/American Heart Association joint committee on clinical practice guidelines. Circulation 145, e895–e1032 (2022). [PubMed: 35363499]

32. Zou KH, Warfield SK, Bharatha A, Tempany CMC, Kaus MR, Haker SJ, Wells WM III Jolesz FA, Kikinis R, Statistical validation of image segmentation quality based on a spatial overlap index. Acad. Radiol 11, 178–189 (2004). [PubMed: 14974593]

33. Sinning J-M, Hammerstingl C, Vasa-Nicotera M, Adenauer V, Lema Cachiguango SJ, Scheer A-C, Hausen S, Sedaghat A, Ghanem A, Müller C, Grube E, Nickenig G, Werner N Aortic regurgitation index defines severity of peri-prosthetic regurgitation and predicts outcome in patients after transcatheter aortic valve implantation. J. Am. Coll. Cardiol 59, 1134–1141 (2012). [PubMed: 22440213]

34. Zoghbi WA, Asch FM, Bruce C, Gillam LD, Grayburn PA, Hahn RT, Inglessis I, Islam AM, Lerakis S, Little SH, Siegel RJ, Skubas N, Slesnick TC, Stewart WJ, Thavendiranathan P, Weissman NJ, Yasukochi S, Zimmerman KG, Guidelines for the evaluation of valvular regurgitation after percutaneous valve repair or replacement. J. Am. Soc. Echocardiogr 32, 431–475 (2019). [PubMed: 30797660]

35. Migliore RA, Adaniya ME, Barranco M, Miramont G, Gonzalez S, Tamagusuku H, Estimation of contraction coefficient of gorlin equation for assessment of aortic valve area in aortic stenosis. World J. Cardiovasc. Dis 07, 119–130 (2017).

36. Taylor R, Evolution of the continuity equation in the doppler echocardiographic assessment of the severity of valvular aortic stenosis. J. Am. Soc. Echocardiogr 3, 326–330 (1990). [PubMed: 2206551]

37. Roche ET, Horvath MA, Wamala I, Alazmani A, Song SE, Whyte W, Machaidze Z, Payne CJ, Weaver JC, Fishbein G, Kuebler J, Vasilyev NV, Mooney DJ, Pigula FA, Walsh CJ, Soft robotic sleeve supports heart function. Sci. Transl. Med 9, eaaf3925 (2017). [PubMed: 28100834]

38. Roche ET, Wohlfarth R, Overvelde JTB, Vasilyev NV, Pigula FA, Mooney DJ, Bertoldi K, Walsh CJ, A bioinspired soft actuated material. Adv. Mater 26, 1200–1206 (2014). [PubMed: 24227698]

39. Rosalia L, Roche E, Saeed MY, in Advances in Cardiovascular Technology, Karimov JH, Fukamachi K, Gillinov M, Eds. (Elsevier, 2022).

40. Bonnemain J, del Nido PJ, Roche ET, Direct cardiac compression devices to augment heart biomechanics and function. Annu. Rev. Biomed. Eng 24, 137–156 (2022). [PubMed: 35395165]

41. Spethmann S, Dreger H, Baldenhofer G, Pflug E, Sanad W, Stangl V, Baumann G, Grubitzsch H, Sander M, Stangl K, Laule M, Knebel F, Long-term doppler hemodynamics and effective orifice areas of Edwards SAPIEN and medtronic CoreValve prostheses after TAVI. Echocardiography 31, 302–310 (2014). [PubMed: 24111700]

42. Asch FM, Vannan MA, Singh S, Khandheria B, Little SH, Allocco DJ, Meredith IT, Feldman TE, Reardon MJ, Weissman NJ, Hemodynamic and echocardiographic comparison of the lotus and

CoreValve transcatheter aortic valves in patients with high and extreme surgical risk. Circulation 137, 2557–2567 (2018). [PubMed: 29530883]

43. Schmidt S, Fortmeier V, Ludwig S, Wienemann H, Körber MI, Lee S, Meertens M, Macherey S, Iliadis C, Kuhn E, Eghbalzadeh K, Bleiziffer S, Baldus S, Schofer N, Rudolph TK, Adam M, Mauri V, Hemodynamics of self-expanding versus balloon-expandable transcatheter heart valves in relation to native aortic annulus anatomy. Clin. Res. Cardiol 111, 1336–1347 (2022). [PubMed: 35704088]

44. Vincent F, Ternacle J, Denimal T, Shen M, Redfors B, Delhaye C, Simonato M, Debry N, Verdier B, Shahim B, Pamart T, Spillemaeker H, Schurtz G, Pontana F, Thourani VH, Pibarot P, Van Belle E, Transcatheter aortic valve replacement in bicuspid aortic valve stenosis. Circulation 143, 1043–1061 (2021). [PubMed: 33683945]

45. Harris AW, Pibarot P, Otto CM, Aortic stenosis: Guidelines and evidence gaps. Cardiol. Clin 38, 55–63 (2020). [PubMed: 31753177]

46. Baumbach H, Ahad S, Rustenbach C, Hill S, Schäufele T, Wachter K, Franke U, Conventional versus transapical aortic valve replacement: Is it time for shift in indications? Thorac. Cardiovasc. Surg 65, 212–217 (2017). [PubMed: 27517166]

47. Muhammad KI, Tokarchik GC, Transcaval transcatheter aortic valve replacement: A visual case review. J. Vis. Surg 4, 102–102 (2018). [PubMed: 29963391]

48. Ruiz-Meana M, Martinson EA, Garcia-Dorado D, Piper HM, Animal ethics in Cardiovascular Research. Cardiovasc. Res 93, 1–3 (2012). [PubMed: 22186604]

49. Rotman OM, Kovarovic B, Sadasivan C, Gruberg L, Lieber BB, Bluestein D, Realistic vascular replicator for TAVR procedures. Cardiovasc. Eng. Technol 9, 339–350 (2018). [PubMed: 29654509]

50. Carter-Storch R, Hansen SM, Dahl JS, Enevold K, Mogensen NSB, Berg H, Clavel M-A, Møller JE, Hemodynamic changes during aortic valve surgery among patients with aortic stenosis. Scand. Cardiovasc. J 56, 276–284 (2022). [PubMed: 35848519]

51. Fukamachi K, Horvath DJ, Karimov JH, Kado Y, Miyamoto T, Kuban BD, Starling RC, Left atrial assist device to treat patients with heart failure with preserved ejection fraction: Initial in vitro study. J. Thorac. Cardiovasc. Surg 162, 120–126 (2021). [PubMed: 32089348]

52. Miyagi C, Kuban BD, Flick CR, Polakowski AR, Miyamoto T, Karimov JH, Starling RC, Fukamachi K, Left atrial assist device for heart failure with preserved ejection fraction: Initial results with torque control mode in diastolic heart failure model. Heart Fail. Rev 10.1007/s10741-021-10117-6 , (2021).

53. Escher A, Choi Y, Callaghan F, Thamsen B, Kertzscher U, Schweiger M, Hübler M, Granegger M, A valveless pulsatile pump for heart failure with preserved ejection fraction: Hemo- and fluid dynamic feasibility. Ann. Biomed. Eng 48, 1821–1836 (2020). [PubMed: 32232694]

54. Rosalia L, Lamberti KK, Landry MK, Leclerc CM, Shuler FD, Hanumara NC, Roche ET, A soft robotic sleeve for compression therapy of the lower limb, Proceedings of the 2021 43rd Annual International Conference of the IEEE Engineering in Medicine & Biology Society, 1 to 5 November 2021, Mexico, pp. 1280–1283.

55. Otto CM, Nishimura RA, Bonow RO, Carabello BA, Erwin JP, Gentile F, Jneid H, Krieger EV, Mack M, McLeod C, O'Gara PT, Rigolin VH, Sundt TM, Thompson A, Toly C, 2020 ACC/AHA guideline for the management of patients with valvular heart disease: A report of the American College of Cardiology/American Heart Association joint committee on clinical practice guidelines. Circulation 143, e72–e227 (2021). [PubMed: 33332150]

56. Lilly LS, Pathophysiology of Heart Disease: A Collaborative Project of Medical Students and Faculty: Fifth Edition, Lilly LS, Ed. (Wolters Kluwer/Lippincott Williams & Wilkins, ed. 6, 2013).
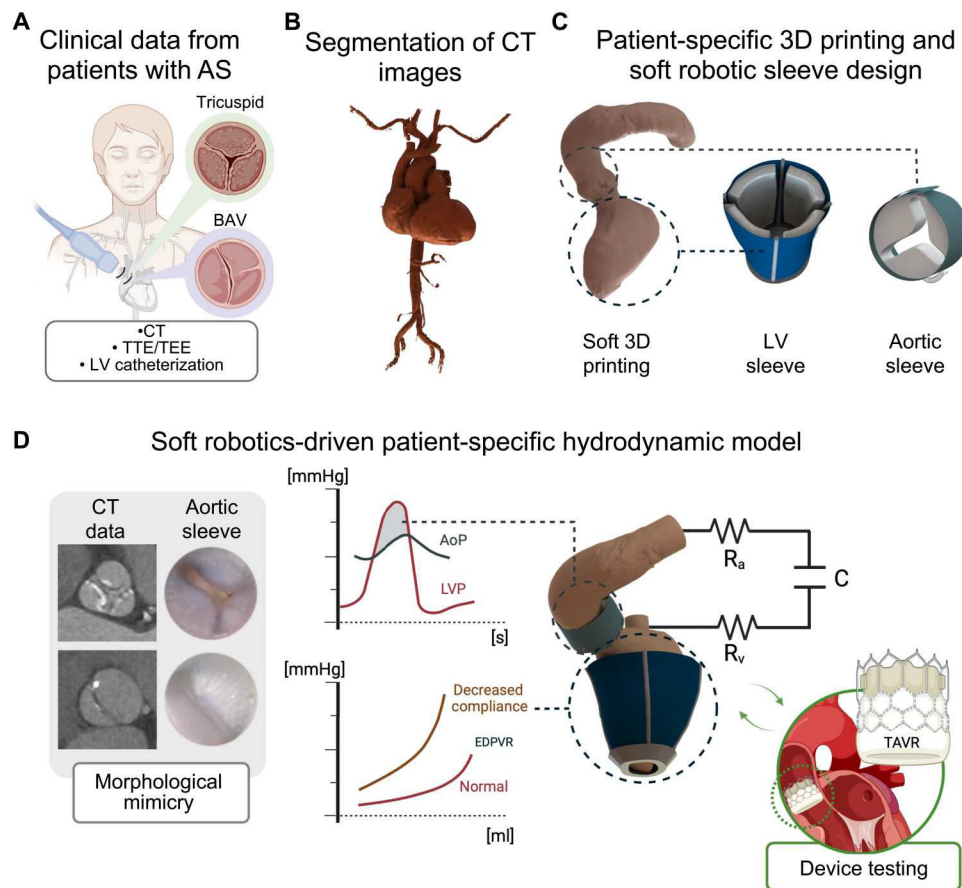
Fig. 1. Architecture of the patient-specific soft robotic hemodynamic model of AS and DD.
(**A**) The model is based on clinical data of patients with AS with diverse anatomies and disease etiologies, such as degenerative tricuspid AS and BAV disease. These patients underwent CT imaging, echocardiography, and, in some instances, LV catheterization. (**B**) Segmentation of the CT images for the design of 3D anatomical models of each patient. (**C**) Key model elements: Soft-material 3D-printed LV and aorta anatomical replicas and patient-specific LV and aortic sleeves. (**D**) Schematic of the soft robotics–driven hydrodynamic model. The system is designed to recreate the patients' hemodynamics and AS morphologies and is ultimately intended as a tool for device evaluation. R_a, arterial resistance; R_v, venous resistance; C, systemic compliance.
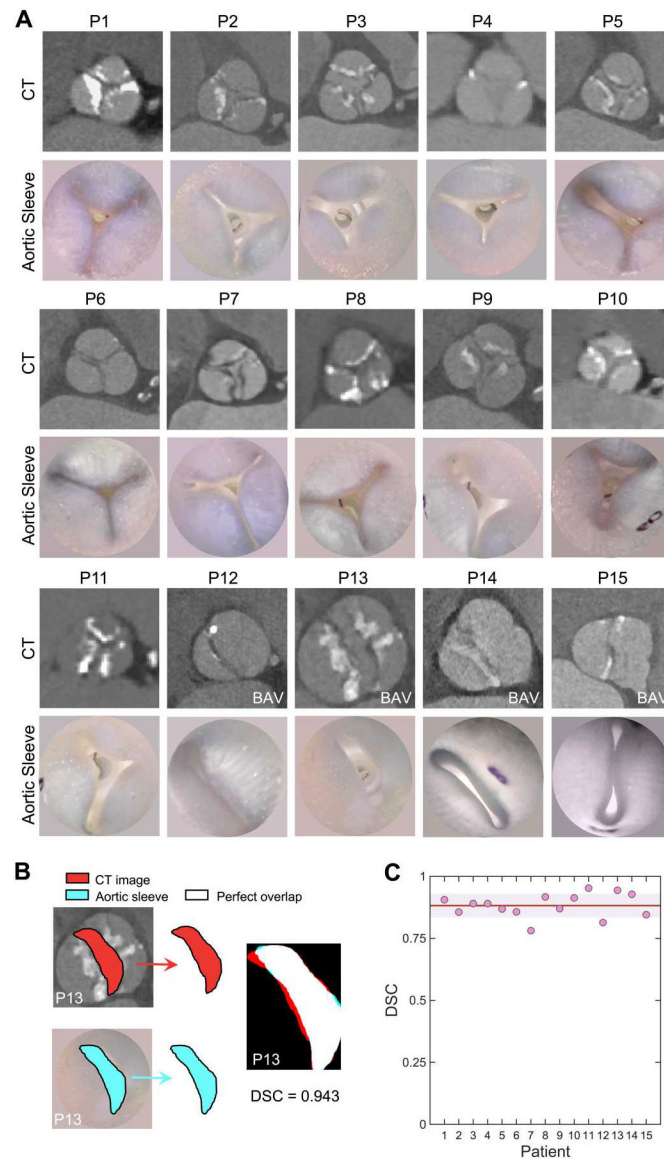
Fig. 2. Morphologic mimicry of the aortic valve defect for both degenerative AS and BAV.
(**A**) Top row: Images of the aortic valve from CT data (patients 1 to 15). Bottom row: Aortic lumen in the model during aortic sleeve actuation. All images taken at peak systole. (**B**) Representative CT and aortic sleeve luminal images (patient 13) for calculation of the DSC. (**C**) DSC for all patients. The red line in the graph denotes the average DSC across the patient population, and the shaded area shows ±1 SD.
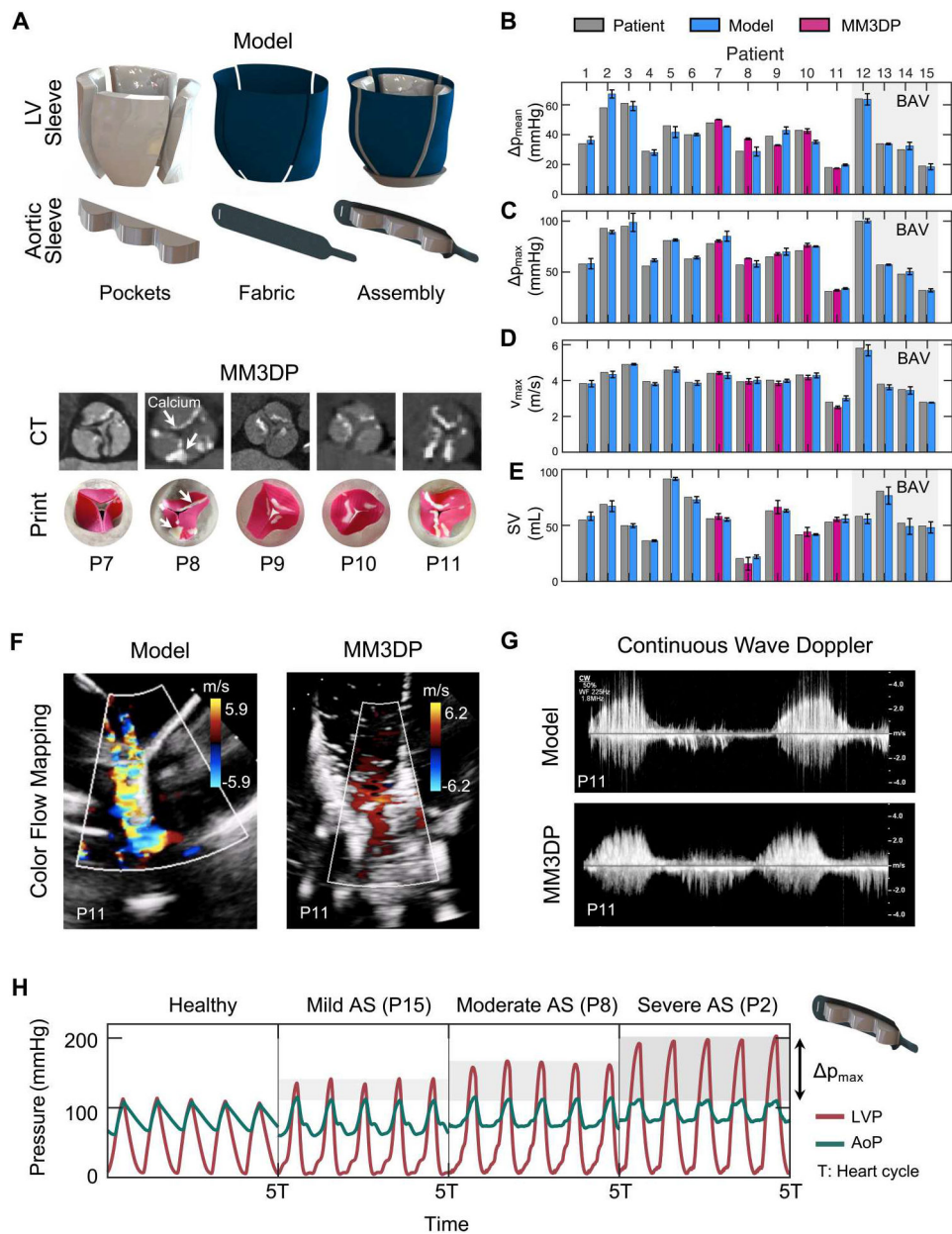
Fig. 3. Soft robotic aortic sleeve recreates clinical metrics of AS.
(**A**) Illustration of the soft robotic and MM3DP modeling approaches. Images of the LV and aortic sleeve components, including the inflatable pockets and inelastic fabric, and of the assembly. Photos of the patient-specific aortic valve leaflets and calcium deposits (white arrows) manufactured using MM3DP technology for patients 7 to 11 and their corresponding CT images. Measurements of (**B**) mean transaortic pressure gradient (P_{mean}, $n = 10$), (**C**) P_{max} ($n = 10$), (**D**) v_{max} ($n = 3$), and (**E**) SV ($n = 10$) for each patient. Each graph shows a comparison between the hemodynamics measured in patients via echography data, the values obtained in our model through actuation of the soft robotic sleeves, and the values obtained using MM3DP. Each error bar represents means $\pm$ 1 SD for n consecutive heart cycles. Representative (**F**) color flow mapping and (**G**) continuous

wave Doppler images for patient 11 obtained by our model and MM3DP. (**H**) Overlaid LVP and AoP waveforms, highlighting changes in P_{max} for representative cases of healthy physiology and of mild (patient 15), moderate (patient 8), and severe (patient 2) AS for $n = 5$ consecutive heart cycles. Healthy waveforms were simulated using a functional bileaflet valve.
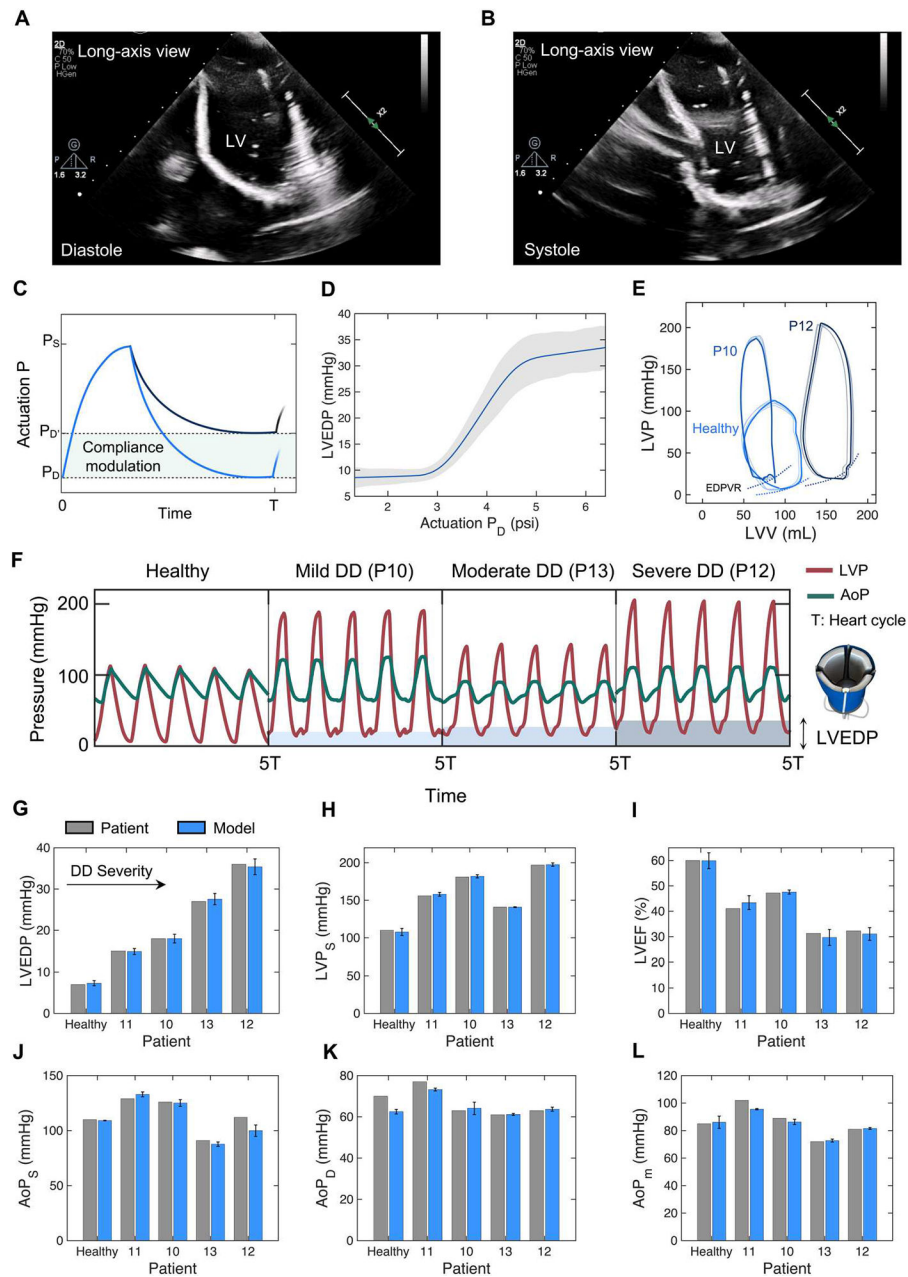
Fig. 4. Patient-specific LV sleeve can be tuned to modulate ventricular elastance and simulate LV remodeling and DD secondary to AS.

Representative echocardiographic images of the soft 3D-printed heart in long-axis view, during actuation by the soft robotic LV sleeve in (**A**) diastole and (**B**) systole. (**C**) Representation of the actuation pressure of the LV sleeve during an entire cardiac cycle, showing that end-diastolic pressure can be tuned to modulate ventricular compliance. P_S, peak systolic actuation pressure; P_D, end-diastolic actuation pressure. (**D**) Changes in LVEDP for various P_D values. (**E**) LV PV loops for representative cases of healthy physiology and of mild (patient 10) and severe (patient 12) DD for $n = 5$ consecutive heart cycles, highlighting changes in the EDPVR. (**F**) Overlaid LVP and AoP waveforms, highlighting changes in LVEDP for representative cases of healthy physiology and of mild

(patient 10), moderate (patient 13), and severe (patient 12) DD and concentric remodeling for $n = 5$ consecutive heart cycles. Catheterization patient data and measured model values of the (**G**) LVEDP, (**H**) LV systolic pressure (LVP$_S$), (I) LVEF, (**J**) AoP$_S$, (**K**) AoP$_D$, and (**L**) AoP$_m$ for the simulated healthy LV and patients with reported catheterization data (patients 11 to 14). Patients were ordered on the basis of DD severity from least (patient 11) to most severe (patient 12). Each error bar represents means $\pm$ 1 SD ($n = 10$ consecutive heart cycles). Average values of healthy LV in (E) to (L) were taken from the literature (7, 56), and healthy waveforms were simulated using a functional bileaflet valve (E to L).
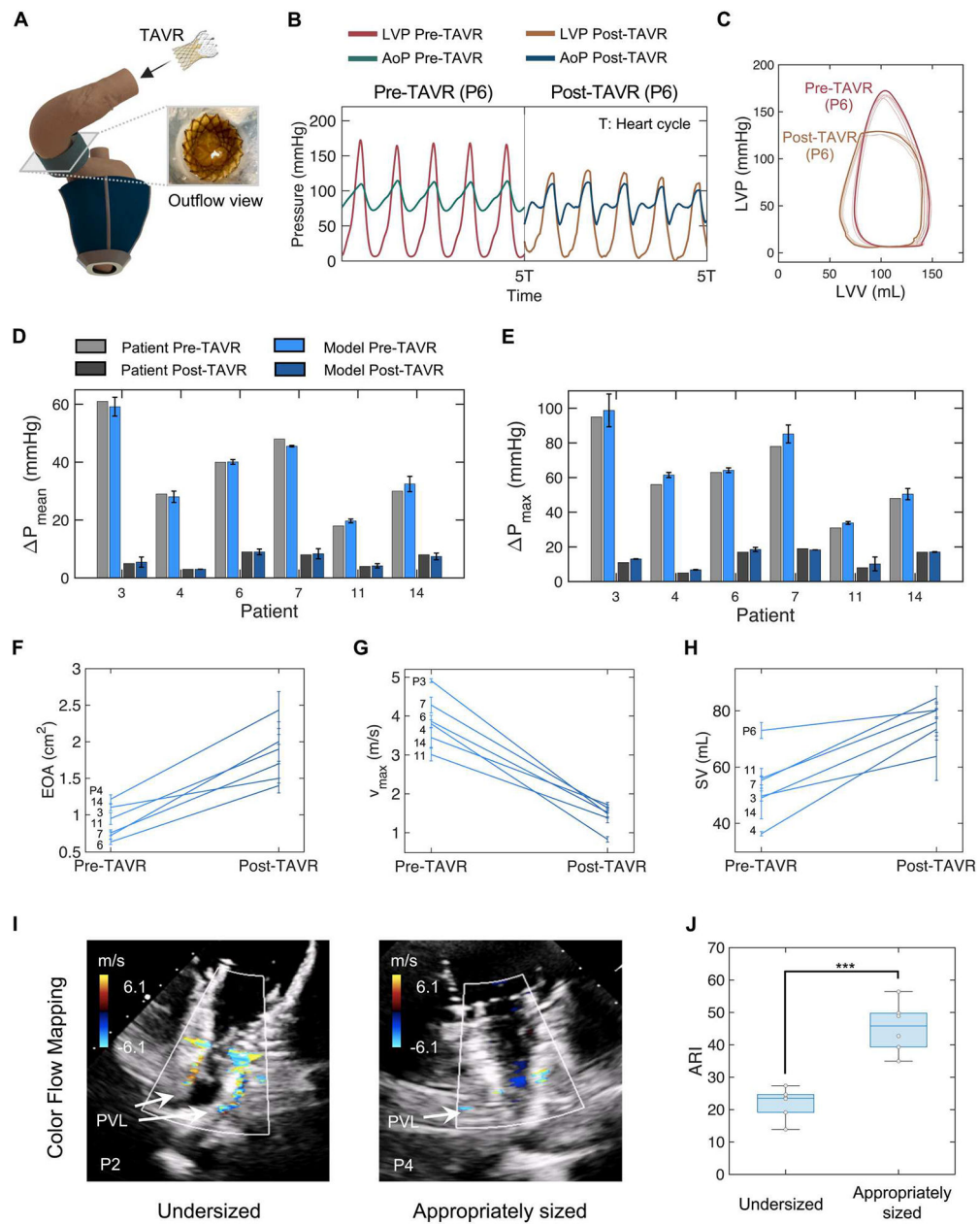
Fig. 5. Comparison of pre- and post-TAVR implantation patient-specific hemodynamics predicted by soft robotic model.

(**A**) Illustration of the 3D-printed heart with soft robotic sleeve and a TAVR being inserted in the system, with a photo of the valve deployed in the aorta. (**B**) Overlaid LVP and AoP waveforms for a representative case (patient 6) of pre- and post-TAVR implantation for n = 5 consecutive heart cycles. (**C**) LV PV loops for the same representative case of pre- and post-TAVR implantation for n = 5 consecutive heart cycles. Pre- and post-implantation measurements (patients 3, 4, 6, 7, 11, and 14) of the (**D**) mean transaortic pressure gradient (P_{mean}) and (**E**) maximum transaortic AoP gradient (P_{max}) and comparison with clinical data. Each error bar represents means ±1 SD (n = 10 consecutive heart cycles). Pre- and post-implantation measurements of the (**F**) EOA (n = 3), (**G**) v_{max} (n = 3), and (**H**) SV (n =

10). (**I**) Representative color flow mapping Doppler images during diastole, highlighting the degree of paravalvular leak for the undersized TAVR (patient 2) and the appropriately sized TAVR (patient 4) scenarios. (**J**) Differences in ARI for the undersized and correctly sized TAVR groups ($P = 9.8 \times 10^{-5}$). Data from $n = 6$ patients per group. t test significance, ***$P < 0.001$.

Movie 1. Overview of the workflow, main findings, and applications of the patient-specific soft robotic model of AS and ventricular remodeling.

Table 1.

Summary of patients' anatomical and hemodynamic characteristics.

F, female; M, male; BSA, body surface area; d, diameter. Thresholds for AS and regurgitation severity (55) and wall thickness (8) from the literature.

Patient	Sex	Age	BSA (m^2)	Annulus d (mm)	Valve anatomy	Severity of stenosis	Regurgitation	Wall thickness	LVEF (%)
1	F	86–90	1.91	24	Tricuspid	Moderate	Trace	Normal	43.2
2	M	91–95	2.05	28	Tricuspid	Severe	Mild	Normal	34.4
3	M	86–90	1.93	23	Tricuspid	Severe	Trace	Increased	40.6
4	F	86–90	1.67	22	Tricuspid	Moderate	Trace	Increased	73.6
5	M	76–80	2.19	25	Tricuspid	Severe	Trace	Increased	71.8
6	M	76–80	2.21	23	Tricuspid	Moderate	Trace	Normal	51.2
7	F	76–80	1.85	25	Tricuspid	Severe	Trace	Normal	44.0
8	M	76–80	2.1	27	Tricuspid	Moderate	No	Increased	29.5
9	F	86–90	1.89	26	Tricuspid	Moderate	Mild	Increased	56.2
10	F	86–90	1.81	24	Tricuspid	Severe	Mild	Increased	47.2
11	F	86–90	1.87	22	Tricuspid	Mild	Trace	Increased	41.1
12	M	51–55	2.23	30	Bicuspid	Severe	Trace	Increased	32.3
13	M	46–50	2.08	32	Bicuspid	Moderate	Trace	Normal	31.3
14	M	66–70	2.20	27	Bicuspid	Moderate	Moderate	Normal	66.0
15	M	76–80	2.15	29	Bicuspid	Mild	Mild	Normal	64.0